

NUMERICAL ANALYSIS AND SCIENTIFIC COMPUTING  
PREPRINT SERIA

**An extended ALE method for  
fluid-structure interaction problems  
with large structural displacements**

S. BASTING    A. QUAINI    S. ČANIĆ    R. GLOWINSKI

PREPRINT #32



DEPARTMENT OF MATHEMATICS  
UNIVERSITY OF HOUSTON

OCTOBER 2014

# An extended ALE method for fluid-structure interaction problems with large structural displacements

Steffen Basting<sup>a</sup>, Annalisa Quaini<sup>b</sup>, Suncica Canic<sup>b</sup>, Roland Glowinski<sup>b</sup>

<sup>a</sup>*Department of Mathematics, Friedrich-Alexander-University Erlangen-Nuremberg,  
Cauerstr. 11, 91058 Erlangen, Germany*

<sup>b</sup>*Department of Mathematics, University of Houston, 4800 Calhoun Rd, Houston TX  
77204, USA*

---

## Abstract

Standard Arbitrary Lagrangian-Eulerian (ALE) methods for the simulation of fluid-structure interaction (FSI) problems fail when the structural displacement is large. We propose an extended ALE method that successfully deals with this problem without remeshing. The extended ALE approach relies on a variational mesh optimization technique, combined with an additional constraint which is imposed to enforce the alignment of the structure with certain edges of the fluid triangulation without changing connectivity. This method is applied to a 2D FSI benchmark problem modeling valves: a thin elastic 1D leaflet, modeled by an inextensible beam equation, is immersed in a 2D incompressible, viscous fluid driven by the time-dependent inlet and outlet data. The fluid and structure are fully coupled via the kinematic and dynamic coupling conditions. The problem is solved using a Dirichlet-Neumann algorithm, which is enhanced by an adaptive relaxation procedure based on Aitken's acceleration. The proposed method is assessed through several numerical tests, including a comparison with a standard ALE method when the structural displacement is small. It is shown that that proposed method deals well with both small and large displacements, and that thanks to the interface alignment, the hydrodynamic force at the interface can be computed accurately.

*Key words:* Mesh optimization, Arbitrary Lagrangian-Eulerian formulation, Fluid-structure interaction, Domain decomposition methods.

---

## 1. Introduction

This paper is concerned with the numerical simulation of the motion of an elastic body immersed in an incompressible, viscous fluid and undergoing large displacements. The motivation comes from fluid-structure interaction (FSI) between blood flow and heart valves. We focus here on a 2D benchmark problem proposed in [17] consisting of a 1D inextensible leaflet interacting with a 2D incompressible fluid. Although dealing with a very simplified model, the problem under consideration retains important physical features common to more

---

*Email addresses:* [basting@math.fau.de](mailto:basting@math.fau.de) (Steffen Basting), [quaini@math.uh.edu](mailto:quaini@math.uh.edu) (Annalisa Quaini), [canic@math.uh.edu](mailto:canic@math.uh.edu) (Suncica Canic), [roland@math.uh.edu](mailto:roland@math.uh.edu) (Roland Glowinski)

complex models: large displacements and added mass effect, which are known to induce various numerical difficulties [44, 12].

Several approaches have been proposed in the literature to simulate FSI problems with large structural displacements, involving valves in particular. We briefly report on the most popular methods, mentioning that the following overview is by no means complete, but is rather meant to give an idea of the variety of methods existing in the literature.

We start with Arbitrary Lagrangian-Eulerian (ALE) approaches [31, 16], since the method proposed in this paper can be classified as an extended ALE approach. A standard ALE approach moves the mesh to follow the elastic body movements. ALE methods were proved to be accurate and robust for hemodynamics applications involving small mesh displacements (see, e.g., [22]). Although these methods offer many advantages provided by the explicit representation of the fluid-structure interface [30, 44, 3], problems arise whenever strong deformations or even topological changes of the interface lead to a degeneration of the computational mesh. Thus, in the presence of large displacements, standard ALE algorithms need frequent remeshing [18, 35, 34], which may introduce an additional source of errors since quantities of interest have to be transferred from the old mesh to the new mesh.

An alternative to ALE methods is provided by methods that are based on fixed meshes. This is the case of the immersed boundary method (see, e.g., [38, 40, 39] and references therein). In this approach, the fluid feels the presence of the structure through external forces (Dirac Delta functions) acting on the fluid. In order to get around the difficulties associated to the discretization of the Dirac Delta, the extended immersed boundary method [47] and the immersed finite element method [49] were introduced. Another method that has been originally designed for fixed meshes is the fictitious domain method [26, 25]. In this method, the coupling is obtained by enforcing the kinematic coupling condition with Lagrange multipliers. The first applications of the fictitious domain method involved the interaction of a fluid with rigid particles. Later, this method has been applied for interactions with flexible structures by using Lagrange multipliers located on the structure surface [2, 29, 45, 46]. Mixed ALE and fictitious domain formulations have also been proposed [28, 17]. In order to give accurate results for the viscous shear stresses on the solid boundary, the fictitious domain method has to be combined with adaptive mesh refinement.

Among other methods used for fluid-structure interactions with large structural displacements, it is worth mentioning an approach based on the level set method [13] and Lattice-Boltzmann methods [32, 21, 19].

The method we propose uses one fixed base mesh that is adapted to approximate the interface while maintaining mesh connectivity (nodes or elements are neither inserted nor removed). We adopt a technique that has been introduced in [48, 7, 6] for two-phase flows and one-way coupled FSI problems (i.e., the structure moves with a prescribed law) and extend it to two-way coupled FSI problems. The fundamental building block of our extended ALE method is a variational mesh optimization approach that does not rely on any combinatorial considerations. Alignment of the optimized mesh with the structure interface is stated as a side constraint of the mesh optimization problem thanks to a level set description of the geometry. Thus, the proposed approach results in a nonlinear, constrained optimization problem.

The main advantages of the proposed extended ALE approach are:

- The alignment of the mesh with the interface, which allows for a simple definition and efficient implementation of problem-specific finite element spaces;
- Fixed mesh connectivity, which makes the method easy to implement in an existing standard ALE code.

Concerning the first point, for the application under consideration the extended ALE allows to easily capture the pressure discontinuity across the interface, which coincides with the 1D leaflet. Methods based on fixed meshes cannot capture such a discontinuity. Moreover, thanks to the mesh alignment with the interface, the kinematic coupling condition is easily enforced.

Once the mesh has been obtained from the above mentioned constrained optimization problem, the FSI problem is solved with a classical Domain Decomposition algorithm, namely, the Dirichlet-Neumann method (see, e.g., [42]), which is combined with an Aitken's acceleration technique [33].

The outline of the paper is as follows. In Section 2 we state the problem. The constrained optimization approach, which is at the core of our extended ALE method, is explained in Section 3. We touch on the numerical methods that we use for the time and space discretization of the fluid, structure, and coupled fluid-structure problems in Section 4. In Section 5, we present numerical results obtained on a carefully chosen series of numerical tests showing the main features of the method. Conclusions are drawn in Section 6.

## 2. Problem definition

Consider a domain  $\Omega \subset \mathbb{R}^2$  containing a thin elastic leaflet forming a 1D manifold  $\Gamma(t) \subset \Omega$  whose location depends on time. The leaflet is surrounded by an incompressible, viscous fluid occupying domain  $\Omega$ , defining the time dependent fluid domain  $\Omega_f(t) := \Omega \setminus \Gamma(t)$ . See Figure 1.

### 2.1. The fluid problem

In the fluid domain, the fluid flow is governed by the Navier-Stokes equations for an incompressible, viscous fluid:

$$\rho_f \left( \frac{\partial \mathbf{u}}{\partial t} + (\mathbf{u} \cdot \nabla) \mathbf{u} \right) - \nabla \cdot \boldsymbol{\sigma} = \mathbf{0} \quad \text{in } \Omega_f(t), \quad (1)$$

$$\nabla \cdot \mathbf{u} = 0 \quad \text{in } \Omega_f(t), \quad (2)$$

for  $t \in [0, T]$ , where  $\rho_f$  is the fluid density,  $\mathbf{u}$  is the fluid velocity, and  $\boldsymbol{\sigma}$  the Cauchy stress tensor. For Newtonian fluids  $\boldsymbol{\sigma}$  has the following expression

$$\boldsymbol{\sigma}(\mathbf{u}, p) = -p\mathbf{I} + 2\mu\boldsymbol{\epsilon}(\mathbf{u}),$$

where  $p$  is the pressure,  $\mu$  is the fluid dynamic viscosity, and  $\boldsymbol{\epsilon}(\mathbf{u}) = (\nabla \mathbf{u} + (\nabla \mathbf{u})^T)/2$  is the strain rate tensor. Equations (1)-(2) need to be supplemented with initial and boundary conditions.

In order to describe the evolution of the fluid domain, we adopt an *Arbitrary Lagrangian-Eulerian* (ALE) approach [31]. Let  $\hat{\Omega}_f \subset \mathbb{R}^2$  be a fixed reference domain. We consider a smooth mapping

$$\begin{aligned} \mathcal{A} &: [0, T] \times \hat{\Omega}_f \rightarrow \mathbb{R}^2, \\ \mathcal{A}(t, \hat{\Omega}_f) &= \Omega_f(t), \quad \forall t \in [0, T]. \end{aligned}$$

For each time instant  $t \in [0, T]$ ,  $\mathcal{A}$  is assumed to be a homeomorphism. The domain velocity  $\mathbf{w}$  is defined as

$$\mathbf{w}(t, \cdot) = \partial_t \mathcal{A}(t, \mathcal{A}(t, \cdot)^{-1}).$$

For any sufficiently smooth function  $F : [0, T] \times \mathbb{R}^2 \rightarrow \mathbb{R}$ , we may define the ALE time derivative of  $F$  as

$$\left. \frac{\partial F}{\partial t} \right|_{\hat{\mathbf{x}}} = \frac{\partial F}{\partial t}(t, \mathcal{A}(t, \hat{\mathbf{x}})) = \frac{\partial F}{\partial t}(t, \mathbf{x}) + \mathbf{w}(t, \mathbf{x}) \cdot \nabla F(t, \mathbf{x})$$

for  $\mathbf{x} = \mathcal{A}(t, \hat{\mathbf{x}})$ ,  $\hat{\mathbf{x}} \in \hat{\Omega}$ . With these definitions, we can write the incompressible Navier-Stokes equations in ALE formulation as follows:

$$\rho_f \left. \frac{\partial \mathbf{u}}{\partial t} \right|_{\hat{\mathbf{x}}} + \rho_f (\mathbf{u} - \mathbf{w}) \cdot \nabla \mathbf{u} - \nabla \cdot \boldsymbol{\sigma} = \mathbf{0} \quad \text{in } \Omega_f(t), \quad (3)$$

$$\nabla \cdot \mathbf{u} = 0 \quad \text{in } \Omega_f(t), \quad (4)$$

for  $t \in [0, T]$ .

## 2.2. The structure problem

The thin leaflet is modeled as an inextensible beam with negligible torsional effects [17]. Let us denote by  $\rho_s$  the linear density (i.e. mass per unit length), by  $L$  the length, and by  $EI$  the flexural stiffness of the beam. The following notation will be used for the spatial and temporal derivatives, with  $s$  denoting arc length and  $t$  time:

$$\mathbf{y}' = \frac{\partial \mathbf{y}}{\partial s}, \quad \dot{\mathbf{y}} = \frac{\partial \mathbf{y}}{\partial t}, \quad \mathbf{y}'' = \frac{\partial^2 \mathbf{y}}{\partial s^2}, \quad \ddot{\mathbf{y}} = \frac{\partial^2 \mathbf{y}}{\partial t^2}.$$

Using the virtual work principle, the beam motion for  $t \in [0, T]$  is modeled by: Find  $\mathbf{x}(t) \in K$ :

$$\int_0^L \rho_s \ddot{\mathbf{x}} \cdot \mathbf{y} ds + \int_0^L EI \mathbf{x}'' \cdot \mathbf{y}'' ds = \int_0^L \mathbf{f} \cdot \mathbf{y} ds, \quad \forall \mathbf{y} \in dK(\mathbf{x}), \quad (5)$$

with

$$K = \{ \mathbf{y} \in (H^2(0, L))^2, |\mathbf{y}'| = 1, \mathbf{y}(0) = \mathbf{a}, \mathbf{y}'(0) = \mathbf{b} \}, \quad (6)$$

$$dK(\mathbf{x}) = \{ \mathbf{y} \in (H^2(0, L))^2, \mathbf{x}' \cdot \mathbf{y}' = 0, \mathbf{y}(0) = \mathbf{0}, \mathbf{y}'(0) = \mathbf{0} \},$$

where  $\mathbf{f}$  denotes the force acting on the beam. In our case  $\mathbf{f}$  is the hydrodynamic force, which will be specified in Subsection 2.3. Condition  $|\mathbf{y}'| = 1$  is the inextensibility condition. It is included in the set  $K$ . Weak formulation (5) assumes that at  $s = L$  natural boundary conditions  $\mathbf{x}''(L) = \mathbf{0}$  and  $\mathbf{x}'''(L) = \mathbf{0}$  are imposed. Note that problem (5) in strong form reads:

$$\begin{aligned} \rho_s \ddot{\mathbf{x}} + EI \mathbf{x}'''' &= \mathbf{f}, \\ |\mathbf{x}'| &= 1. \end{aligned}$$

The problem is supplemented with initial conditions.

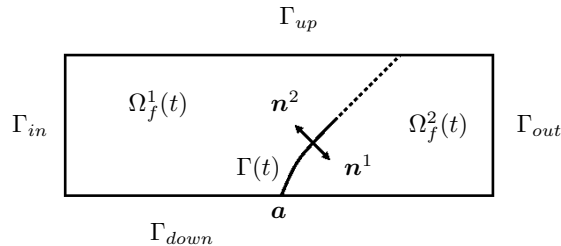


Figure 1: The leaflet  $\Gamma(t)$  separates the fluid domain  $\Omega_f(t)$  into subdomains  $\Omega_f^1(t)$  and  $\Omega_f^2(t)$ .

### 2.3. The coupled fluid-structure interaction problem

The leaflet moves due to the contact force exerted by the fluid. Ideally, the location of the leaflet determines two subdomains  $\Omega_f^1(t)$  and  $\Omega_f^2(t)$ , such that  $\Omega_f(t) = \Omega_f^1(t) \cup \Omega_f^2(t)$ , and  $\Gamma(t)$  belongs to a portion of the boundary joining  $\Omega_f^1(t)$  and  $\Omega_f^2(t)$ , see Fig. 1. Let  $\mathbf{n}^1$  and  $\mathbf{n}^2$  be the outward normals at  $\Gamma(t)$  on  $\Omega_f^1(t)$  and  $\Omega_f^2(t)$ , respectively. See Fig. 1.

The hydrodynamic force acting on the leaflet is given by

$$\mathbf{f}_\Gamma = -\boldsymbol{\sigma}^1 \mathbf{n}^1 - \boldsymbol{\sigma}^2 \mathbf{n}^2. \quad (7)$$

For  $t \in [0, T]$ , the fluid problem (3),(4) and the structure problem (5) are coupled by two conditions:

1. kinematic coupling condition (continuity of velocity, i.e., the no-slip condition)

$$\mathbf{u} = \dot{\mathbf{x}} \quad \text{on } \Gamma(t); \quad (8)$$

2. dynamic coupling condition (balance of contact forces)

$$\mathbf{f}_\Gamma = \mathbf{f} \quad \text{on } \Gamma(t), \quad (9)$$

where  $\mathbf{f}$  is given by Eq. (5).

Here, notation  $\mathbf{u} = \dot{\mathbf{x}}$  in (8) is used to express the relation  $\mathbf{u}(t, \mathbf{x}(t, s)) = \dot{\mathbf{x}}(t, s)$ ,  $s \in [0, L]$  (analogously for  $\mathbf{f}_\Gamma$  and  $\mathbf{f}$  in (9)).

Notice that since the structure domain has one dimension less than the fluid domain, the fluid-structure interface coincides with the structure domain.

### 3. Numerical Representation of the Geometry

The ALE approach we use to deal with large displacements of the leaflet was introduced in [48, 7, 6] for one-way coupled fluid-structure interaction problems and two-phase flows. Here, we extend this approach to two-way coupled FSI problems. The main feature of this method is a variational mesh optimization technique combined with an additional constraint to enforce the alignment of the structure interface with edges of the resulting triangulation. A method with similar properties was introduced in [9]. The alignment procedure proposed therein is based on explicit combinatorial considerations to approximate the interface using the fluid mesh. In contrast, the approach we use here does not rely on any combinatorial consideration. In the following, we present a brief outline of our approach.

### 3.1. Optimal triangulations

Let  $\mathcal{T}$  be an initial triangulation of the domain  $\Omega$  (not necessarily approximating the structure interface at this stage). Following a variational mesh optimization technique introduced by M. Rumpf in [43], we aim at finding an “optimal” triangulation  $\mathcal{T}^*$  resulting from an optimal mesh deformation  $\varphi^*$  of  $\mathcal{T}$ , i.e.  $\mathcal{T}^* = \varphi^*(\mathcal{T})$ . Deformation  $\varphi^*$  belongs to the set  $D$  of piecewise affine, orientation preserving, and globally continuous deformations:

$$D = \{\varphi \in \mathcal{C}^0(\Omega) : \nabla\varphi|_T \in \text{GL}(2), \det(\nabla\varphi|_T) > 0, \forall T \in \mathcal{T}\},$$

with  $\text{GL}(2) = \{A \in \mathbb{R}^{2 \times 2} : \det(A) \neq 0\}$ .

Deformation  $\varphi^* \in D$  is “optimal” in the sense that it is the argument for which a certain functional  $\mathcal{F}$  attains its minimum value:

$$\mathcal{F}(\varphi^*) = \min_{\varphi \in D} \mathcal{F}(\varphi). \quad (10)$$

We assume that the functional in (10) can be represented by a sum of weighted, element-wise contributions  $F_T$ :

$$\mathcal{F}(\varphi) = \sum_{T \in \mathcal{T}} \mu_T F_T(\varphi),$$

where  $\mu_T > 0$  denotes a positive weight with  $\sum_T \mu_T = 1$ . Let  $R_T$  denote the linear reference mapping from a prescribed reference element  $T^*$  (an equilateral simplex with customizable edge length  $h$ ) to  $T$ . Under the assumptions of translational invariance, isotropy and frame indifference of the functionals, it can be shown (see [43]) that in two dimensions  $F_T$  may be expressed as a function of the invariants  $\|\nabla R_T(\varphi)\|^2$  and  $\det(\nabla R_T(\varphi))$ . Here,  $\|\cdot\|$  denotes the Frobenius norm. Note that the quantity  $\|\nabla R_T(\varphi)\|^2$  measures the change of edge lengths with respect to the reference element, and  $\det(\nabla R_T(\varphi))$  measures the change in area.

In order to rule out deformations with vanishing determinant, we need

$$\lim_{\det(\nabla R_T(\varphi)) \rightarrow 0} F_T(\varphi) = \infty.$$

A classical example of function  $F_T$  is given by

$$F_T(\varphi) = (\|\nabla R_T(\varphi)\|^2 - 2)^2 + \det(\nabla R_T(\varphi)) + \frac{1}{\det(\nabla R_T(\varphi))}. \quad (11)$$

The optimally deformed simplex is obtained if  $\varphi^*|_T = \mathbf{I}$ , i.e. if

$$F_T(\varphi^*) = F_T(\mathbf{I}) = (2 - 2)^2 + 1 + 1 = 2.$$

The variational mesh smoothing approach described above has several advantages:

- Minimization problem (10) yields triangulations which are optimal in the sense of the local measure (11);
- These triangulations can be shown to be non-degenerate, i.e. no self-intersection of elements occurs;
- The element-wise representation of  $\mathcal{F}$  provides built-in, local mesh quality control.

The price to pay for those advantages is that functional  $\mathcal{F}$  in (10) is highly non-linear, non-convex, and global minimizers may be non-unique.

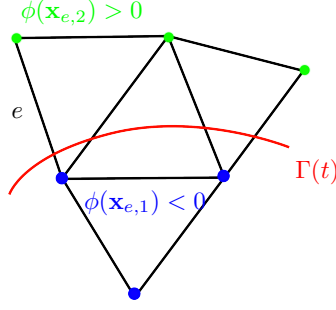


Figure 2:  $\Gamma(t)$  intersecting elements of the fluid mesh.

### 3.2. Interface aligned mesh

We are now interested in having a triangulation that is optimal (as explained in the previous subsection) *and* aligned with the leaflet position  $\Gamma(t)$ , i.e. we want the optimal triangulation edges to approximate  $\Gamma(t)$ . To this purpose, we introduce as an auxiliary tool, a continuous level set function  $\phi : [0, T] \times \Omega \rightarrow \mathbb{R}$  which implicitly defines the structure position  $\mathbf{x}$  by its zero level set:

$$\begin{aligned}\Omega_f^1(t) &= \{\mathbf{y} \in \Omega : \phi(t, \mathbf{y}) > 0\}, \\ \Omega_f^2(t) &= \{\mathbf{y} \in \Omega : \phi(t, \mathbf{y}) < 0\}, \\ \Gamma(t) &= \{\mathbf{y} \in \Omega : \phi(t, \mathbf{y}) = 0\}.\end{aligned}\tag{12}$$

Let us consider the situation reported in Fig. 2: let  $e$  be an arbitrary edge of the triangulation  $\mathcal{T}$  intersected by  $\Gamma(t)$ , and let  $\mathbf{x}_{e,1}$  and  $\mathbf{x}_{e,2}$  be its endpoints. Due to continuity of  $\phi$  and assumption (12), we conclude that

$$\phi(\mathbf{x}_{e,1})\phi(\mathbf{x}_{e,2}) < 0$$

if and only if  $e$  is intersected by  $\Gamma(t)$ , provided that the mesh size  $h$  is sufficiently small to resolve the shape of  $\Gamma(t)$ . We therefore define the triangulation to be *linearly aligned* with  $\Gamma(t)$  if

$$\phi(\mathbf{x}_{e,1})\phi(\mathbf{x}_{e,2}) \geq 0 \quad \text{for all } e \in \mathcal{T}.$$

We define a scalar constraint

$$\begin{aligned}c &: D \rightarrow \mathbb{R}_0^+, \\ c(\varphi) &= \sum_{e \in \varphi(\mathcal{T})} \mathcal{H}(\phi(\mathbf{x}_{e,1})\phi(\mathbf{x}_{e,2})) \quad \text{where} \\ \mathcal{H}(z) &= \begin{cases} > 0 & \text{if } z < 0, \\ = 0 & \text{otherwise.} \end{cases}\end{aligned}$$

Only deformations  $\varphi$  for which  $c(\varphi) = 0$  will give aligned triangulations. Thus, a linearly aligned triangulation of optimal quality is obtained from the following constrained optimization problem:

$$\min_{\varphi \in D} \mathcal{F}(\varphi) \quad \text{such that } c(\varphi) = 0.$$

For details on the numerical realization of the above problem, we refer the reader to [7, 48].

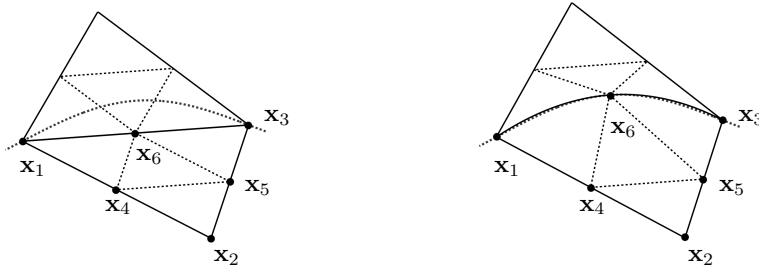


Figure 3: Linearly aligned triangulation with isoparametric elements without (left) and with (right) quadratic alignment of the additional quadratic degree of freedom  $\mathbf{x}_6$ .

Given an aligned triangulation  $\mathcal{T}$ , we may define a linear approximation of the interface as

$$\Gamma_h = \{\text{edges } e \in \mathcal{T} : \phi(\mathbf{x}_{e,i}) = 0 \text{ for } i = 1, 2\}.$$

In order to obtain a more accurate representation of the leaflet position, we also consider piecewise quadratic approximations of  $\Gamma(t)$ . We make use of isoparametric elements equipped with additional degrees of freedom located at the edges. We denote by  $\hat{K} = \{\hat{\mathbf{x}} \in \mathbb{R}^2 : \sum_{i=1}^2 \hat{x}^{(i)} \leq 1, \hat{x}^{(i)} \geq 0\}$  the reference simplex, and by  $G_K : \hat{K} \rightarrow K$  the quadratic isoparametric mapping:

$$G_K(\hat{\mathbf{x}}) = \sum_{i=1}^6 \mathbf{x}_i \varphi_i(\hat{\mathbf{x}}), \quad (13)$$

where  $\varphi_i, i = 1, \dots, 6$  are the quadratic Lagrange basis functions. Once a linearly aligned triangulation  $\mathcal{T}^*$  and the corresponding discrete interface are obtained, in order to achieve quadratic alignment we move each quadratic node (e.g.,  $\mathbf{x}_6$  in Figure 3) along the linear normal to the zero level set.

Details on the numerical realization together with an evaluation of the mesh, approximation quality, and computational costs can be found in [7, 4, 48].

**Remark 1.** *In order to reduce computational costs, the mesh optimization is performed only in a box bounding the leaflet, instead of the whole domain. The bounding box moves with the leaflet and is such that the leaflet never intersects its boundary. Outside the box, the mesh is unaffected by leaflet motion.*

#### 4. Discretization

In this section, we describe our strategy for the numerical solution of the FSI problem (3),(4),(5),(8),(9). In Section 4.1 we discuss the method we choose to solve the coupled problem, while the methods adopted for the space and time discretization of the fluid and structure sub-problems are presented in Sections 4.2 and 4.3, respectively. We also report on how the hydrodynamic force (7) is computed.

#### 4.1. A partitioned approach for the coupled FSI problem

For the solution of the coupled problem, we choose a classical Domain Decomposition method, called the Dirichlet-Neumann algorithm (see, e.g., [42]). This algorithm is based on the evaluation of independent fluid and structure problems, coupled via the coupling (transmission) conditions (8) and (9) in an iterative fashion: the Dirichlet boundary condition (8) is imposed on the interface for the fluid sub-problem, whereas the structure sub-problem is supplemented with the Neumann boundary condition (9).

Let  $\Delta t$  be a time discretization step and set  $t^n = n\Delta t$ , for  $n = 1, \dots, N$ , with  $N = T/\Delta t$ . At every time  $t^n$ , the Dirichlet-Neumann algorithm iterates over the fluid and structure sub-problems until convergence. These are Richardson (also called fixed point) iterations for the position of  $\Gamma(t^n)$ . Let  $k$  be the index for these iterations. At time  $t^{n+1}$ , iteration  $k+1$ , the following steps are performed:

- Step 1: Solve the fluid sub-problem for the flow variables  $\mathbf{u}_{k+1}, p_{k+1}$  defined on  $\Omega_{f,k}$ , with Dirichlet boundary condition  $\mathbf{u}_{k+1} = \hat{\mathbf{x}}_k$  on  $\Gamma_k$ .
- Step 2: Solve the structure sub-problem for the structure position  $\mathbf{x}_{k+1}$ , driven by the just calculated hydrodynamic force  $\mathbf{f}_{\Gamma,k+1}$ , i.e.,  $\mathbf{f}_{k+1} = \mathbf{f}_{\Gamma,k+1}$  on  $\Gamma_k$ , and obtain  $\Gamma_{k+1}$ , which defines  $\Omega_{f,k+1}$ .
- Step 3: Check the stopping criterion, e.g.

$$\frac{\|\mathbf{x}_{k+1} - \mathbf{x}_k\|}{\|\mathbf{x}_k\|} < \epsilon_{DN}, \quad (14)$$

where  $\epsilon_{DN}$  is a given stopping tolerance. For instance, for the tests in Sec. 5, we set  $\epsilon_{DN} = 10^{-8}$ .

If the stopping criterion is satisfied, we set  $\mathbf{u}^{n+1} = \mathbf{u}_{k+1}$ ,  $p^{n+1} = p_{k+1}$ ,  $\mathbf{x}^{n+1} = \mathbf{x}_{k+1}$ ,  $\Gamma^{n+1} = \Gamma_{k+1}$ , and  $\Omega_f^{n+1} = \Omega_{f,k+1}$ ; otherwise we go back to step 1.

**Remark 2.** *Due to the high computational costs associated with numerical minimization, we perform the mesh optimization algorithm described in Sec. 3.2 only once per time step (for  $k = 1$ ), that is only after the Dirichlet-Neumann method has converged in the previous time step. For subiterations  $k > 1$ , we do not update the fluid mesh, but keep  $\Omega_{f,k} = \Omega_{f,0}$ .*

The evident advantage of the Dirichlet-Neumann method is modularity: it allows to reuse existing fluid and structure solvers with minimum effort. Unfortunately, the convergence properties of the Dirichlet-Neumann algorithm depend heavily on the added-mass effect [12]. In fact, it is known that when the structure lies on part of the fluid domain boundary the number of Dirichlet-Neumann iterations required to satisfy the stopping criterion (14) increases as the structure density approaches the fluid density. Moreover, below a certain density ratio  $\rho_s/\rho_f$ , which depends on the domain geometry, relaxation is needed for the Dirichlet-Neumann algorithm to converge (see, e.g., [36, 37, 12]).

To this end, we adopt the relaxation parameters given by a simple Aitken's acceleration technique, which is known to reduce the number of Dirichlet-Neumann iterations. This strategy, introduced in [33], was proposed for a setting similar to ours in [1].

Let  $\tilde{\mathbf{x}}_{k+1}$  be the unrelaxed structure position predicted by Step 2 of the Richardson iteration above. Then after Step 2, we introduce a relaxation parameter  $\omega_{k+1}$ , which is computed via

$$\omega_{k+1} = \frac{(\mathbf{x}_k - \mathbf{x}_{k-1}) \cdot (\mathbf{x}_k - \tilde{\mathbf{x}}_{k+1} - \mathbf{x}_{k-1} + \tilde{\mathbf{x}}_k)}{|\mathbf{x}_k - \tilde{\mathbf{x}}_{k+1} - \mathbf{x}_{k-1} + \tilde{\mathbf{x}}_k|^2}.$$

The position of the interface is then corrected via the relaxation algorithm:

$$\mathbf{x}_{k+1} = \omega_{k+1} \tilde{\mathbf{x}}_{k+1} + (1 - \omega_{k+1}) \mathbf{x}_k.$$

It was found in [1] that only a few accelerated Dirichlet-Neumann sub-iterations are to be expected for FSI problems with an immersed structure. We will comment on the required number of subiterations in Section 5.3.

We are currently implementing a different partitioned scheme (see, e.g., [11]) which might have better performance and stability properties when the fluid and structure have comparable densities. The current work will serve as a benchmark for further computational method developments in this area.

#### 4.2. The discrete fluid sub-problem

Let us start by writing the weak formulation for problem (3),(4) supplemented with boundary condition (8). We will state the problem in weak form by including only the boundary condition on  $\Gamma(t)$ , since those on  $\partial\Omega_f(t) \setminus \Gamma(t)$  are understood and do not affect the presented method.

For any given  $t \in [0, T)$ , we define the following spaces:

$$\begin{aligned} V(t) &= \left\{ \mathbf{v} : \Omega_f(t) \rightarrow \mathbb{R}^2, \mathbf{v} = \hat{\mathbf{v}} \circ (\mathcal{A})^{-1}, \hat{\mathbf{v}} \in (H^1(\hat{\Omega}_f))^2 \right\}, \\ V_0(t) &= \left\{ \mathbf{v} \in V(t), \mathbf{v}|_{\Gamma(t)} = \mathbf{0} \right\}, \\ Q(t) &= \left\{ q : \Omega_f(t) \rightarrow \mathbb{R}, q = \hat{q} \circ (\mathcal{A})^{-1}, \hat{q} \in L^2(\hat{\Omega}_f) \right\}. \end{aligned}$$

In the following we will use the notation  $V_k := V(t_k)$  and  $Q_k := Q(t_k)$  to denote the finite element spaces at the time instant  $t_k$ .

We introduce the following linear forms:

$$\begin{aligned} m(\Omega; \mathbf{u}, \mathbf{v}) &= \int_{\Omega} \rho_f (\mathbf{u} \cdot \mathbf{v}) \, d\Omega, \\ a(\Omega; \mathbf{u}, \mathbf{v}) &= \int_{\Omega} \mu (\boldsymbol{\epsilon}(\mathbf{u}) : \boldsymbol{\epsilon}(\mathbf{v})) \, d\Omega, \\ c(\Omega; \mathbf{u}; \mathbf{v}, \mathbf{w}) &= \int_{\Omega} \rho_f ((\mathbf{u} \cdot \nabla) \mathbf{v} \cdot \mathbf{w}) \, d\Omega, \\ b(\Omega; p, \mathbf{v}) &= - \int_{\Omega} p \nabla \cdot \mathbf{v} \, d\Omega. \end{aligned}$$

The variational formulation of the fluid problem (3),(4) with boundary condition (8) reads: given  $t \in (0, T]$ , find  $(\mathbf{u}, p) \in V(t) \times Q(t)$  such that  $\forall (\mathbf{v}, q) \in V_0(t) \times Q(t)$  the following holds:

$$\begin{aligned} m\left(\Omega_f(t); \frac{\partial \mathbf{u}}{\partial t} \Big|_{\tilde{\mathbf{x}}}, \mathbf{v}\right) + c(\Omega_f(t); \mathbf{u} - \mathbf{w}; \mathbf{u}, \mathbf{v}) + a(\Omega_f(t); \mathbf{u}, \mathbf{v}) + b(\Omega_f(t); p, \mathbf{v}) &= \mathbf{0} \\ b(\Omega_f(t); q, \mathbf{u}) &= 0, \\ \mathbf{u}|_{\Gamma(t)} &= \tilde{\mathbf{x}}. \end{aligned}$$

**Time and space discretization.** We approximate in time the above weak problem by the backward differentiation formula of order 1 or 2 (BDF1 or BDF2) and we linearize the convective term by an extrapolation formula of the same order. At time  $t^{n+1}$ , and at the  $(k+1)$ -st Dirichlet-Neumann sub-iteration, the time discrete linearized fluid sub-problem reads as follows: Find  $(\mathbf{u}_{k+1}, p_{k+1}) \in V_k \times Q_k$  such that

$$\begin{aligned} m\left(\Omega_{f,k}; \partial_{\Delta t} \mathbf{u}_{k+1} \Big|_{\hat{\mathbf{x}}}, \mathbf{v}\right) + a(\Omega_{f,k}; \mathbf{u}_{k+1}, \mathbf{v}) + b(\Omega_{f,k}; p_{k+1}, \mathbf{v}) \\ + c(\Omega_{f,k}; \mathbf{u}^* - \mathbf{w}^*; \mathbf{u}_{k+1}, \mathbf{v}) = 0, \quad (15) \\ b(\Omega_{f,k}; q, \mathbf{u}_{k+1}) = 0, \quad (16) \\ \mathbf{u}_{k+1} = \hat{\mathbf{x}}_k \quad \text{on } \Gamma_k, \quad (17) \end{aligned}$$

for all  $(\mathbf{v}, q) \in V_{0,k} \times Q_k$ , where

$$\begin{aligned} \text{BDF1: } \partial_{\Delta t} \mathbf{u}_{k+1} \Big|_{\hat{\mathbf{x}}} &= \frac{\mathbf{u}_{k+1} - \mathbf{u}^n}{\Delta t}, \quad \mathbf{u}^* = \mathbf{u}^k, \quad \mathbf{w}^* = \mathbf{w}^k, \\ \text{BDF2: } \partial_{\Delta t} \mathbf{u}_{k+1} \Big|_{\hat{\mathbf{x}}} &= \frac{3\mathbf{u}_{k+1} - 4\mathbf{u}^n + \mathbf{u}^{n-1}}{2\Delta t}, \quad \mathbf{u}^* = 2\mathbf{u}^k - \mathbf{u}^{k-1}, \quad \mathbf{w}^* = 2\mathbf{w}^k - \mathbf{w}^{k-1}. \end{aligned}$$

For the space discretization of problems (15)-(17), we choose the inf-sup stable Taylor-Hood finite element pair  $\mathbb{P}_2 - \mathbb{P}_1$ . However, while the velocity field is continuous at  $\Gamma_k$ , the pressure space should be able to capture discontinuities across  $\Gamma_k$ , which are needed also for the correct evaluation of the hydrodynamic force (7). In order to deal with pressure discontinuities that occur at  $\Gamma_k$  (recall that  $\Gamma_k$  belongs to a portion of the boundary between domains  $\Omega_{f,k}^1$  and  $\Omega_{f,k}^2$ ), we introduce the following spaces:

$$\begin{aligned} \tilde{V}_k^h &= \left\{ \mathbf{v} \in (H^1(\Omega_{f,k}))^2 : \mathbf{v}|_K \circ G_K^2 \in \mathbb{P}_2(\hat{K}), \mathbf{v}|_{\Omega_{f,k}^i} \in (C^0(\Omega_{f,k}^i))^2, i = 1, 2 \right\}, \\ \tilde{V}_{0,k}^h &= \left\{ \mathbf{v} \in \tilde{V}_k^h : \mathbf{v}|_{\Gamma_k} = \mathbf{0} \right\}, \\ \tilde{Q}_k^h &= \left\{ q \in L^2(\Omega_{f,k}), q|_K \circ G_K \in \mathbb{P}_1(\hat{K}), q|_{\Omega_{f,k}^i} \in C^0(\Omega_{f,k}^i), i = 1, 2 \right\}, \end{aligned}$$

where  $\hat{K}$  is the reference simplex, and  $G_K$  is given by (13). The respective continuous spaces will be denoted by  $V_k^h$ ,  $V_{0,k}^h$ , and  $Q_k^h$ . The appropriate finite element space for the unknowns in problems (15)-(17) is given by  $V_k^h \times \tilde{Q}_k^h$ .

For the numerical implementation of our approach, we adopt a strategy called Subspace Projection Method [8, 6, 41]: we will work with spaces  $\tilde{V}_k^h$  and  $\tilde{Q}_k^h$ , and then use an additional discrete projection to enforce continuity for the velocity on  $\Gamma_k$ . Note that  $V_k^h$  is a vector subspace of space  $\tilde{V}_k^h$ .

To make this precise, we first notice that Oseen problem (15) can be formally expressed as: Find  $(\mathbf{u}_{k+1}, p_{k+1}) \in V_k \times Q_k$  such that

$$s((\mathbf{u}_{k+1}, p_{k+1}), (\mathbf{v}, q)) = g(\mathbf{v}, q), \quad \forall (\mathbf{v}, q) \in V_{0,k} \times Q_k, \quad (18)$$

where  $s : (V_k \times Q_k) \times (V_{0,k} \times Q_k) \rightarrow \mathbb{R}$  is the bilinear form containing all the terms with index  $k+1$ , and  $g : (V_k \times Q_k) \rightarrow \mathbb{R}$  is a linear form containing all the terms involving known quantities. Then, we can define a projection operator:

$$\mathcal{P} : \tilde{V}_k^h \rightarrow V_k^h,$$

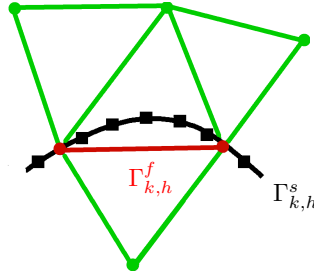


Figure 4: Fluid triangulation (green) aligned with the structure mesh  $\Gamma_{k,h}^s$  (black). The fluid nodes are marked with dots, while the structure nodes are marked with squares.  $\Gamma_{k,h}^f$  (red) is the approximation of the interface given by the fluid mesh.

where  $V_k^h$  is a vector subspace of space  $\tilde{V}_k^h$ . By the Subspace Projection Method, a discrete counterpart of problem (18) reads: Find  $(\tilde{\mathbf{u}}_{k+1}^h, \tilde{p}_{k+1}^h) \in \tilde{V}_k^h \times \tilde{Q}_k^h$  such that

$$s((\mathcal{P}\tilde{\mathbf{u}}_{k+1}^h, \tilde{p}_{k+1}^h), (\mathcal{P}\tilde{\mathbf{v}}^h, \tilde{q}^h)) = g(\mathcal{P}\tilde{\mathbf{v}}^h, \tilde{q}^h), \quad \forall (\tilde{\mathbf{v}}^h, \tilde{q}^h) \in \tilde{V}_{0,k}^h \times \tilde{Q}_k^h,$$

and then set the continuous velocity  $\mathbf{u}^h = \mathcal{P}\tilde{\mathbf{u}}^h$ .

The linear system resulting from linearization and discretization is solved with a direct solver (UMFPACK [15, 14]).

**Enforcement of the kinematic coupling condition, i.e., the Dirichlet condition (17).** Recall that at every Dirichlet-Neumann sub-iteration  $k$ , the fluid mesh is aligned with the structure position found at the previous iteration  $n$  (see Remark 2). However, in general the fluid and structure meshes do *not* coincide since they are made up of different elements (cubic Hermite elements on the structure side, and quadratic isoparametric edges on the fluid side). This creates a problem when enforcing the kinematic coupling condition, i.e., Dirichlet condition (17) in the fluid problem. However, *due to the alignment of fluid mesh with the structure* at time  $t^n$ , fluid nodes which approximate the interface are always located on the structure mesh, see Figure 4. Therefore, to approximate the value of the structure velocity at the fluid nodes (in case they are not identical), we can simply interpolate the structure velocity at the fluid nodes and set that approximate structure velocity equal to the fluid velocity at those nodes to implement the kinematic coupling condition.

More precisely, we take the following approach. Denote by  $\Gamma_{k,h}^f$  the approximation of the location of  $\Gamma_k = \Gamma^n$  given by the fluid mesh, and by  $\Gamma_{k,h}^s$  the approximation of  $\Gamma_k = \Gamma^n$  by the structure mesh, see Figure 4. Denote by  $U_{\Gamma,k}$  and  $\dot{X}_k$  the arrays of the nodal values of the corresponding fluid and structure velocities at the interface. Let us denote by  $B_{fs,k}$  the interpolation matrix of the structure mesh at the fluid interface nodes. To impose Dirichlet condition (17), we set

$$U_{\Gamma,k+1} = B_{fs,k}\dot{X}_k. \quad (19)$$

#### 4.3. The discrete structure sub-problem

**Time and space discretization.** For the time discretization of problem (5), we will consider a generalized Crank-Nicolson scheme (see, e.g., [27]). At

time  $t^{n+1}$ , and Dirichlet-Neumann sub-iteration  $k+1$ , the time discrete structure sub-problem is as follows: Find  $\mathbf{x}_{k+1} \in K$  such that:

$$\begin{aligned} & \int_0^L \rho_s \frac{\mathbf{x}_{k+1} - 2\mathbf{x}^n + \mathbf{x}^{n-1}}{\Delta t^2} \cdot \mathbf{y} ds + \int_0^L EI(\alpha \mathbf{x}_{k+1} + (1-2\alpha)\mathbf{x}^n + \alpha \mathbf{x}^{n-1})'' \cdot \mathbf{y}'' ds \\ &= \int_0^L (\alpha \mathbf{f}_{k+1} + (1-2\alpha)\mathbf{f}^n + \alpha \mathbf{f}^{n-1}) \cdot \mathbf{y} ds, \end{aligned} \quad (20)$$

for all  $\mathbf{y} \in dK(\mathbf{x}_{k+1})$ , where  $dK(t)$  is defined in (6). Here  $\mathbf{x}_{k+1}$  refers to the approximated structure position at the time step  $n+1$ , Dirichlet-Neumann iteration  $k+1$ .

This scheme is known to be second order accurate for linear problems. For the numerical results in Sec. 5, we will set  $\alpha = 1/4$  since it is known that for linear cases this choice leads to an unconditionally stable scheme which possesses a very small numerical dissipation compared to other schemes, e.g., the Houbolt method [10]. Our results in [5] show that even for our nonlinear problem, this choice of  $\alpha$  works well.

Time discretization approximates problem (5) by a sequence of quasi-static problems. Each quasi-static problem is equivalent to the following minimization problem

$$\mathbf{x}_{k+1} = \arg \min_{\mathbf{y} \in K} J(\mathbf{y}), \quad (21)$$

where the total energy of the beam can be written as:

$$J(\mathbf{y}) = \frac{1}{2} \int_0^L \frac{\rho_s}{\Delta t^2} |\mathbf{y}|^2 ds + \frac{1}{2} \int_0^L EI \alpha |(\mathbf{y})''|^2 ds - \int_0^L \tilde{\mathbf{f}}_{k+1} \cdot \mathbf{y} ds,$$

with  $\tilde{\mathbf{f}}_{k+1}$  accounting for the forcing terms and the terms resulting from time discretization (i.e. terms involving the solution at previous time steps).

To treat the inextensibility condition  $|\mathbf{y}'| = 1$ , which is a quadratic constraint, we use an augmented Lagrangian Method (see, e.g., [10, 23, 24, 27]). Let us introduce the following spaces and sets:

$$\begin{aligned} \mathcal{V} &= \{ \mathbf{y} \in (H^2(0, L))^2, \mathbf{y}(0) = \mathbf{a}, \mathbf{y}'(0) = \mathbf{b} \}, \\ \mathcal{V}_0 &= \{ \mathbf{y} \in (H^2(0, L))^2, \mathbf{y}(0) = \mathbf{0}, \mathbf{y}'(0) = \mathbf{0} \}, \\ \mathcal{Q} &= \{ \mathbf{q} \in (L^2(0, L))^2, |\mathbf{q}| = 1 \text{ a.e. on } (0, L) \}, \end{aligned}$$

Problem (21) is equivalent to

$$\{ \mathbf{x}_{k+1}, \mathbf{x}'_{k+1} \} = \arg \min_{\{ \mathbf{y}, \mathbf{q} \} \in W} J(\mathbf{y}), \quad \text{with } W = \{ \mathbf{y} \in \mathcal{V}, \mathbf{q} \in \mathcal{Q}, \mathbf{y}' - \mathbf{q} = \mathbf{0} \}.$$

For  $r > 0$ , we introduce the following augmented Lagrangian functional:

$$\mathcal{L}_r(\mathbf{y}, \mathbf{q}; \boldsymbol{\mu}) = J(\mathbf{y}) + \frac{r}{2} \int_0^L |\mathbf{y}' - \mathbf{q}|^2 ds + \int_0^L \boldsymbol{\mu} \cdot (\mathbf{y}' - \mathbf{q}) ds. \quad (22)$$

Let  $\{ \mathbf{x}, \mathbf{p}; \boldsymbol{\lambda} \}$  be a saddle point of  $\mathcal{L}_r$  over  $(\mathcal{V} \times \mathcal{Q}) \times (L^2(0, L))^2$ . Then  $\mathbf{x}$  is a solution of problem (21) and  $\mathbf{p} = \mathbf{x}'$ . In order to solve the above saddle-point problem, we employ the algorithm called ALG2 studied, e.g., in [23, 27], which

is in fact a ‘disguised’ Douglas-Rachford operator-splitting scheme. It reads as follows.

Take an initial guess  $\{\mathbf{x}^{-1}, \boldsymbol{\lambda}^0\} \in \mathcal{V} \times (L^2(0, L))^2$ . Then, for  $i \geq 0$ ,  $\{\mathbf{x}^{i-1}, \boldsymbol{\lambda}^i\}$  being known, proceed with:

Step 1: Find  $\mathbf{p}^i \in \mathcal{Q}$  such that:

$$\mathcal{L}_r(\mathbf{x}^{i-1}, \mathbf{p}^i; \boldsymbol{\lambda}^i) \leq \mathcal{L}_r(\mathbf{x}^{i-1}, \mathbf{q}; \boldsymbol{\lambda}^i), \quad \forall \mathbf{q} \in \mathcal{Q}. \quad (23)$$

Step 2: Find  $\mathbf{x}^i \in \mathcal{V}$  such that:

$$\mathcal{L}_r(\mathbf{x}^i, \mathbf{p}^i; \boldsymbol{\lambda}^i) \leq \mathcal{L}_r(\mathbf{y}, \mathbf{p}^i; \boldsymbol{\lambda}^i), \quad \forall \mathbf{y} \in \mathcal{V}_0. \quad (24)$$

Step 3: Update the Lagrange multipliers by:

$$\boldsymbol{\lambda}^{i+1} = \boldsymbol{\lambda}^i + r((\mathbf{x}^i)' - \mathbf{p}^i). \quad (25)$$

For details on how to solve the minimization problems at Steps 1 and 2 we refer the reader to [10, 23, 24, 5]. For the space discretization of problem (20), we use a third order Hermite finite element method (see, e.g., [10]).

Steps 1, 2, and 3 are repeated until the following stopping criterion

$$\left( \int_0^L \left| \frac{\partial}{\partial s} \mathbf{x}^i - \mathbf{p}^i \right|^2 ds \right)^{1/2} \leq \epsilon_{\text{inex}} \quad (26)$$

is satisfied for a given tolerance  $\epsilon_{\text{inex}} > 0$ , or the number of iterations exceeds a given number.

**Remark 3.** *It is known that parameter  $r$  plays a fundamental role for the convergence of algorithm (23)-(25), as was pointed out in [17]. We adopt the same adaptive strategy presented in [17], i.e. we start with an initial guess  $r = r_0$ , where  $r_0$  is a fixed number (for instance in the range of the flexural stiffness  $EI$ ). Once the Augmented Lagrangian algorithm terminates, we check if termination criterion (26) is met. In case (26) is violated, the value of  $r$  is increased (e.g., by a factor of 10) and ALG2 is repeated with the new value of  $r$ .*

Once (26) is satisfied, we set  $\tilde{\mathbf{x}}_{k+1} = \mathbf{x}^i$ , which defines the new structure position before relaxation.

**Remark 4.** *Numerical experiments in [5] show that the generalized Crank-Nicolson scheme with  $\alpha = 1/4$  is of second order when solving the inextensible beam problem with ALG2, provided that the stopping tolerance for the Augmented Lagrangian method is sufficiently small.*

**Enforcement of the dynamic coupling condition, i.e, the fluid load onto the structure.** The fluid load onto the structure is given by the hydrodynamic force (7). The computation of the hydrodynamic force (7) is crucial for the numerical stability and accuracy of the Dirichlet-Neumann FSI solver (see, e.g., [20]). In the setting considered in this paper (an immersed leaflet), the quality of approximation of the pressure jump across the leaflet is of great importance, as demonstrated by the results in Section 5.1.

The load exerted by the fluid onto the structure  $\mathbf{f}_\Gamma$  can be computed as the variational residual  $\mathcal{R}$  of the momentum conservation equation for the fluid, tested with test functions  $\mathbf{v}$  that are different from zero at  $\Gamma(t)$ :

$$\begin{aligned}
\int_{\Gamma(t)} \mathbf{f}_\Gamma \cdot \mathbf{v} \, d\Gamma &= - \int_{\Gamma(t)} \boldsymbol{\sigma}^1 \mathbf{n}^1 \cdot \mathbf{v} \, d\Gamma - \int_{\Gamma(t)} \boldsymbol{\sigma}^2 \mathbf{n}^2 \cdot \mathbf{v} \, d\Gamma \\
&= - \left( \Omega_f^1(t); \frac{\partial \mathbf{u}}{\partial t} \Big|_{\bar{\mathbf{x}}}, \mathbf{v} \right) - c(\Omega_f^1(t); \mathbf{u} - \mathbf{w}; \mathbf{u}, \mathbf{v}) - a(\Omega_f^1(t); \mathbf{u}, \mathbf{v}) - b(\Omega_f^1(t); p, \mathbf{v}) \\
&\quad - \left( \Omega_f^2(t); \frac{\partial \mathbf{u}}{\partial t} \Big|_{\bar{\mathbf{x}}}, \mathbf{v} \right) - c(\Omega_f^2(t); \mathbf{u} - \mathbf{w}; \mathbf{u}, \mathbf{v}) - a(\Omega_f^2(t); \mathbf{u}, \mathbf{v}) - b(\Omega_f^2(t); p, \mathbf{v}) \\
&= \mathcal{R}(\Omega_f^1(t); \mathbf{u}, p, \mathbf{v}) + \mathcal{R}(\Omega_f^2(t); \mathbf{u}, p, \mathbf{v}). \tag{27}
\end{aligned}$$

Let  $\mathbf{f}_{\Gamma, k+1}^f$  denote the discrete hydrodynamic force at  $\Gamma_{k,h}^f$ . After time and space discretization of (27),  $\mathbf{f}_{\Gamma, k+1}^f$  is calculated from:

$$\begin{aligned}
\int_{\Gamma_{k,h}^f} \mathbf{f}_{\Gamma, k+1}^f \cdot \mathbf{v}_h \, d\Gamma &= \mathcal{R}(\Omega_{f,k}^1; \mathbf{u}_{k+1}^h, p_{k+1}^h, \mathbf{v}_h) \\
&\quad + \mathcal{R}(\Omega_{f,k}^2; \mathbf{u}_{k+1}^h, p_{k+1}^h, \mathbf{v}_h), \tag{28}
\end{aligned}$$

where  $\mathbf{u}_{k+1}^h$  and  $p_{k+1}^h$  are the discrete velocity and pressure at the Dirichlet-Neumann sub-iteration  $k+1$ , obtained from solving system (15)-(17) with  $\mathbf{v}_h \in V_k^h$ . By using matrix notation, this problem can be written as follows:

$$M_{\Gamma, k}^f F_{\Gamma, k+1}^f = R_{k+1}, \tag{29}$$

where  $F_{\Gamma, k+1}^f$  is the array of nodal values of  $\mathbf{f}_{\Gamma, k+1}^f$ ,  $M_{\Gamma, k}^f$  is the mass matrix at  $\Gamma_{k,h}^f$ , and  $R_{k+1}$  corresponds to the known values of the combined residuals appearing on the right-hand side of equation (28). This defines the hydrodynamic force, calculated at the fluid mesh nodes along the leaflet.

To enforce the dynamic coupling condition (9), this hydrodynamic force needs to be set equal to the structural load  $\mathbf{f}$  on the leaflet. Since the fluid and structure meshes do not match, we are facing the same difficulty as in evaluating the kinematic coupling condition (i.e., the Dirichlet condition) in the fluid sub-problem. To get around this difficulty, we assign the values of the hydrodynamic force at the structure mesh nodes  $\Gamma_{k,h}^s$  in the following way.

Denote by  $F_{\Gamma, k+1}^s$  the values of the hydrodynamic force at the structure mesh nodes  $\Gamma_{k,h}^s$ . To calculate  $F_{\Gamma, k+1}^s$  we first project the structure mesh nodes  $\Gamma_{k,h}^s$  onto the fluid mesh  $\Gamma_{k,h}^f$  at the interface. This can be done easily since the two meshes are aligned (although not matching). Then, evaluate  $\mathbf{f}_{\Gamma, k+1}^f$  at the projected structure nodes using interpolation. Denoting by  $B_{sf, k}$  the interpolation matrix of the projected structure nodes on  $\Gamma_{k,h}^f$ , we define

$$F_{\Gamma, k+1}^s = B_{sf, k} F_{\Gamma, k+1}^f. \tag{30}$$

This defines the hydrodynamic force at the *structure mesh nodes*, and enforces the dynamic coupling condition (9).

**Power exchange.** It is important to notice that in this numerical implementation of the dynamic coupling condition, the power exchanged between the

fluid and structure is not perfectly balanced, i.e., at the discrete level, the energy imparted by the fluid onto the structure is not perfectly converted into the total energy of the structure, and vice versa. This is due to the non-matching fluid and structure meshes. Never the less, as we show in Sec. 5.2, the difference between the two is "negligible". This can be precisely quantified as follows.

At the time  $t^{n+1}$ , after the convergence of the Dirichlet-Neumann sub-iterations, the discrete power exchanged at the interface from the fluid side is

$$\begin{aligned} P^{f,n+1} &= \int_{\Gamma_h^{f,n+1}} \mathbf{f}_\Gamma^{f,n+1} \cdot \mathbf{u}_h^{n+1} \, d\Gamma = (U_\Gamma^{n+1})^T M_\Gamma^{f,n+1} F_\Gamma^{f,n+1} \\ &= (\dot{X}^{n+1})^T (B_{fs}^{n+1})^T M_\Gamma^{f,n+1} F_\Gamma^{f,n+1}, \end{aligned} \quad (31)$$

where for the last equation we used (19). Similarly, the discrete power exchanged at the interface from the structure side is

$$\begin{aligned} P^{s,n+1} &= \int_{\Gamma_h^{s,n+1}} \mathbf{f}_\Gamma^{s,n+1} \cdot \dot{\mathbf{x}}_h^{n+1} \, d\Gamma = (\dot{X}^{n+1})^T M_\Gamma^{s,n+1} F_\Gamma^{s,n+1} \\ &= (\dot{X}^{n+1})^T M_\Gamma^{s,n+1} B_{sf}^{n+1} F_\Gamma^{f,n+1}, \end{aligned} \quad (32)$$

where for the last equation we used (30). Thus, the power exchanged at the interface is balanced if

$$(B_{fs}^{n+1})^T M_\Gamma^{f,n+1} = M_\Gamma^{s,n+1} B_{sf}^{n+1}.$$

Since  $\Gamma_h^{f,n+1}$  and  $\Gamma_h^{s,n+1}$  are aligned but do not coincide ( $\Gamma_h^{s,n+1}$  is a piecewise cubic, globally  $C^1$  function and  $\Gamma_h^{f,n+1}$  is a piecewise quadratic interpolation) and the fluid and structure discretizations are based on different elements, the balance equation is not necessarily fulfilled exactly. However, in Sec. 5.2 we will show that the difference between  $P^{f,n+1}$  and  $P^{s,n+1}$  is very small in our computations.

## 5. Numerical results

We performed a series of numerical tests aimed at assessing our extended ALE approach and showing its features. In all the tests, we consider the following:

- **Geometry:** A rectangular fluid domain of height 1 cm and length 6 cm:  $[-3, 3] \text{ cm} \times [-0.5, 0.5] \text{ cm}$  is considered. The thin "valve leaflet" is clamped at the midpoint of the base, and it is 0.5 cm long.
- **Boundary conditions:** A no slip condition is imposed on  $\Gamma_{down}$  (see Fig. 1), a symmetry condition is imposed on  $\Gamma_{up}$ , and a homogeneous Neumann condition is enforced on  $\Gamma_{out}$ . The inlet condition changes depending on the test.

The fluid density  $\rho_f$  is set to 1 g/cm<sup>3</sup>, while the dynamic viscosity  $\mu$  varies to achieve a peak Reynolds number (based on the maximum inlet velocity  $U$ ) equal to 100 in each test. The structure properties will be specified in each test case.

We will consider different **meshes** for the fluid domain, while for the structure space discretization we take  $h_s = 0.5/44$  cm in every test. The time step is always set to  $10^{-2}$  s. For the Augmented Lagrangian method in Sec. 4.3, we take  $\epsilon_{inez} = 10^{-4}$  in (26), and at the beginning of the simulation we set  $r_0 = 10^{-4}$ .

### 5.1. Test 1: Continuous vs. discontinuous pressure across the interface

The goal of this preliminary test is to show the importance of capturing the pressure discontinuity across the interface. For this purpose we consider a simple test problem which involves a steady state solution. This solution is obtained after a time-independent Poiseuille profile is imposed at  $\Gamma_{in}$  with maximum velocity  $U = 1$  cm/s, and the initial position of the leaflet is a vertical straight line. We set  $\rho_s = 10^6$  g/cm and  $EI = 0.01$  g/(cm s<sup>2</sup>). For the given inlet condition and structural parameters, the leaflet displacement is negligible ( $\simeq 10^{-5}$  cm) during the time interval  $[0, 10]$  s. See Figure 6.

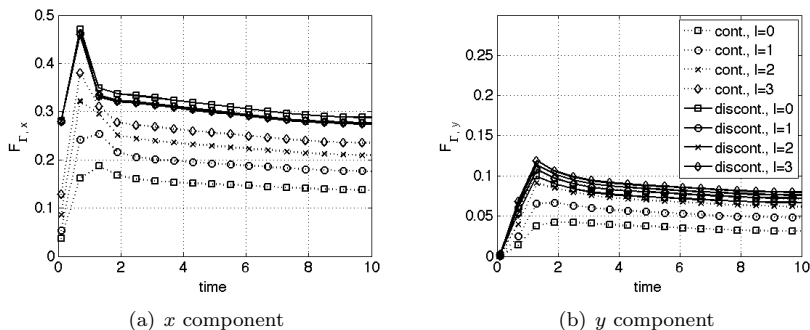


Figure 5: Integral over the interface of the components of the hydrodynamic force over time: (a)  $x$  component and (b)  $y$  component. The results are obtained on four different meshes ( $l = 0, 1, 2, 3$ ) and with finite element pairs  $V_k^h \times Q_k^h$  (continuous pressure) and  $V_k^h \times \tilde{Q}_k^h$  (discontinuous pressure). The legend in (b) is common to both subfigures.

We consider four meshes resulting from uniform refinement of an initial coarse mesh for the fluid subdomain, with edge lengths  $h_f = \sqrt{2}/8 \cdot 2^{-l}$  cm,  $l = 0, 1, 2, 3$ . We track the behavior of the hydrodynamic force along the leaflet over time to see the convergence behavior of both pressure approximations. Namely, we track, in time, the  $x$  and  $y$  components of the integrated hemodynamic force (“averaged force”) over the interface:

$$F_{\Gamma,x}(t) = \int_{\Gamma_h^s(t)} \mathbf{f}_{\Gamma,x}^f(t) \, d\Gamma, \quad F_{\Gamma,y}(t) = \int_{\Gamma_h^s(t)} \mathbf{f}_{\Gamma,y}^f(t) \, d\Gamma.$$

In Fig. 5, we plot  $F_{\Gamma,x}$  and  $F_{\Gamma,y}$  for all four meshes and finite element pairs  $V_k^h \times Q_k^h$  corresponding to the *continuous pressure* case, and all for meshes and finite element pairs  $V_k^h \times \tilde{Q}_k^h$  corresponding to the *discontinuous pressure* case. The following conclusions can be reached from this study:

- In all the cases, both components reach a plateau after roughly 8 s, meaning that a steady state has been “achieved” at that time, i.e., a steady state is well approximated by the solution at time 8 s.

- When using the  $V_k^h \times \tilde{Q}_k^h$  pair, corresponding to the discontinuous pressure approximation, mesh independence is reached at the third mesh refinement, while for the  $V_k^h \times Q_k^h$  pair, mesh independence is not achieved even after four mesh refinements.
- At each successive refinement the solution values computed with continuous pressure get closer to the solution values computed with the discontinuous pressure on coarse mesh. Thus, the  $V_k^h \times Q_k^h$  pair requires a *significantly finer mesh* to approximate the physical solution as well as the discontinuous pressure pair  $V_k^h \times \tilde{Q}_k^h$ .

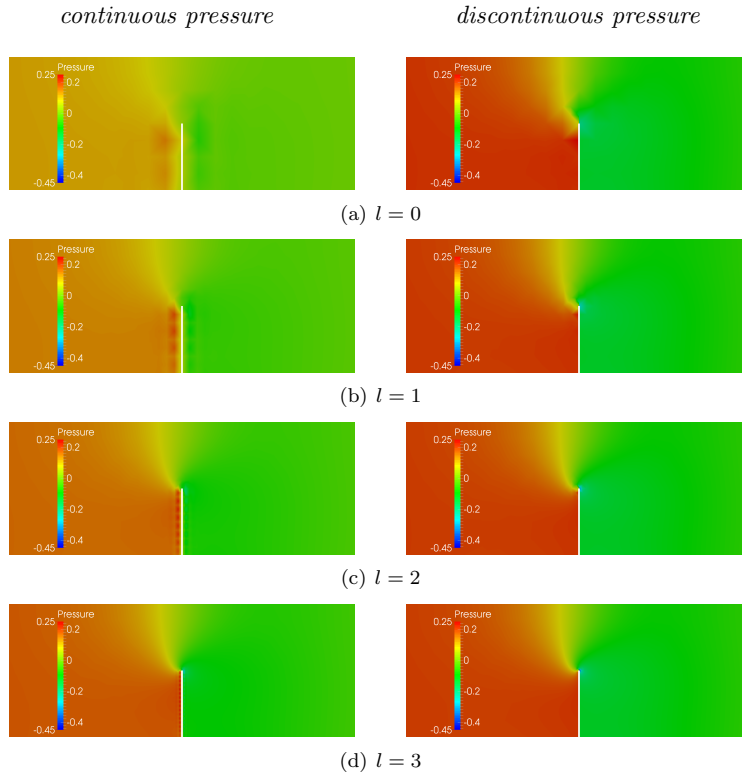


Figure 6: Pressure in a portion of the computational domain at time  $t = 9$  s computed with the continuous (left) and discontinuous (right) pressure finite element pair on four different refinement levels: (a)  $l = 0$ , (b)  $l = 1$ , (c)  $l = 2$ , and (d)  $l = 3$ .

As a qualitative evidence, we report in Fig. 6 the pressure at time  $t = 9$  s computed on the four meshes with both finite element pairs. One can see that when using the continuous pressure, there is a huge difference between the pressure computed on the coarsest mesh and the pressure computed on the finest mesh. This is not the case when using the discontinuous pressure finite element pair. Moreover, the continuous pressure computed on the finest mesh looks clearly similar to the discontinuous pressure on any mesh.

From now on, we present the results which have all been obtained with the  $V_k^h \times \tilde{Q}_k^h$  pair.

5.2. Test 2: Standard ALE vs. extended ALE for small structure displacements

With this test we aim at showing that when the structure displacement is relatively small, the solution obtained using our extended ALE approach “coincides” with the solution obtained using the standard ALE approach. For this purpose, we consider a time-dependent (time periodic) problem which is driven by the inlet velocity data, which is a time-dependent Poiseuille velocity profile, with maximum velocity:

$$U(t) = \frac{1}{4} \left( 1 - \cos\left(\frac{\pi}{2}t\right) \right) \text{ cm/s.}$$

The Strouhal number for this problem is 0.5, and we set  $\rho_s = 5 \text{ g/cm}$  and  $EI = 0.05 \text{ g/(cm s}^2\text{)}$ . The inlet boundary condition and the structural parameters were chosen to generate a “moderate”-amplitude oscillatory motion of the beam around its initial configuration, which is a straight vertical line.

We consider two meshes for the fluid subdomain with  $h_f = \sqrt{2}/8 \cdot 2^{-l} \text{ cm}$ ,  $l = 1, 2$ , and apply our extended ALE method and a standard ALE method on both meshes. We study: (1) the quantitative comparison of the location of the beam tip, i.e., its  $x$  coordinate, vs. time, (2) the qualitative comparison of the solution in the 2D channel, superimposed over the fluid mesh, and (3) the quantitative comparison between the two methods of the power exchanged at the interface. The following conclusions are obtained:

- The oscillations of the beam tip computed with the two methods are perfectly in phase both for mesh  $l = 1$  and  $l = 2$ . See Figure 7. While there is a slight difference in amplitude with mesh  $l = 1$  (the movement computed with the standard ALE method is slightly smaller), the movements of the beam tip computed with the two approaches on mesh  $l = 2$  are superimposed over the whole time interval  $[0, 10]$  s.
- A qualitative comparison of the beam position, together with the fluid velocity magnitude, computed with the standard and extended ALE methods at time  $t = 7.9$  s is reported in Fig. 8. In Fig. 8, we also show the computational mesh at the selected times: we can see the difference in the mesh deformation given by the standard ALE method and our extended ALE approach. We remind that in the latter case the mesh is optimal in the sense of the local measure (11).
- Excellent agreement between the values of the discrete power exchanged at the interface between the two methods can be seen in Fig. 9. More precisely, Fig. 9 shows the discrete power exchanged at the interface from the fluid side  $P^f$ , defined in (31), computed with the two ALE approaches on meshes  $l = 1, 2$ . We see occasional jumps in the discrete power computed with the extended ALE approach. Those jumps occur when a node passes from the fluid domain (either  $\Omega_f^1(t)$  or  $\Omega_f^2(t)$ ) to the interface, or vice versa, and they become smaller as the mesh gets finer (compare Fig. 9(a) and 9(b)). A further quantification of the power exchange error is presented at the end of this section.

**Mesh independence.** We show that the results reported in Figs. 7 and 9 are mesh independent. We consider three different fluid domain meshes with  $h_f = \sqrt{2}/8 \cdot 2^{-l} \text{ cm}$ ,  $l = 0, 1, 2$ . The  $x$  component of the beam tip vs. time, computed with the standard ALE method on the three different meshes over the

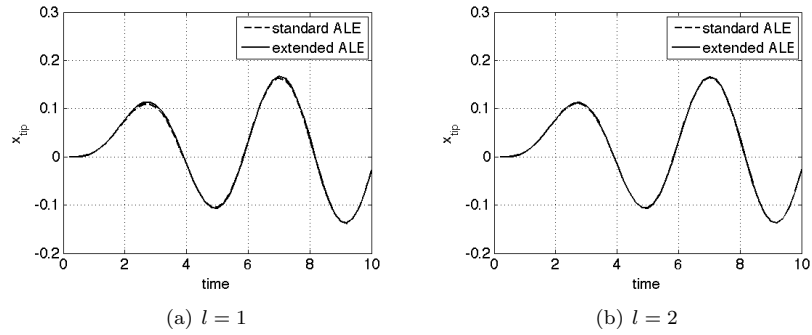


Figure 7: Comparison of the  $x$  component of the beam tip movement computed with a standard ALE and the extended ALE method on mesh  $l = 1$  (a), and on mesh  $l = 2$  (b).

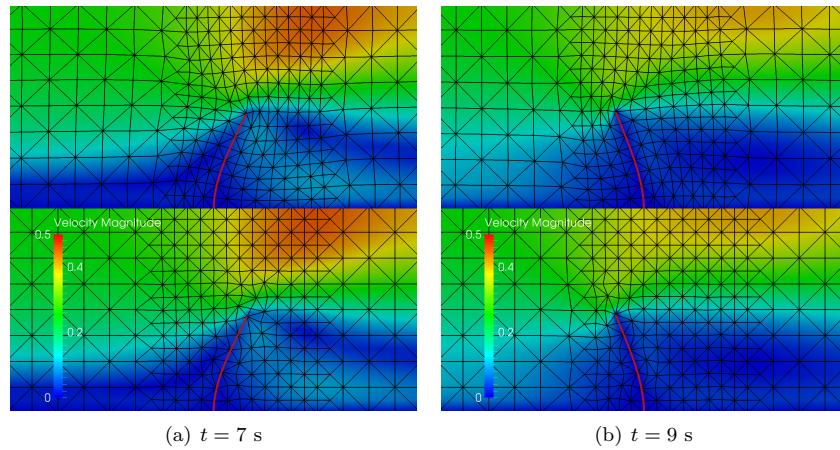


Figure 8: Test 2: Fluid velocity magnitude and beam position computed with a standard ALE approach (top) and the extended ALE method (bottom) at the time  $t = 7$  s (a), and at  $t = 9$  s (b). The computational mesh is also shown.

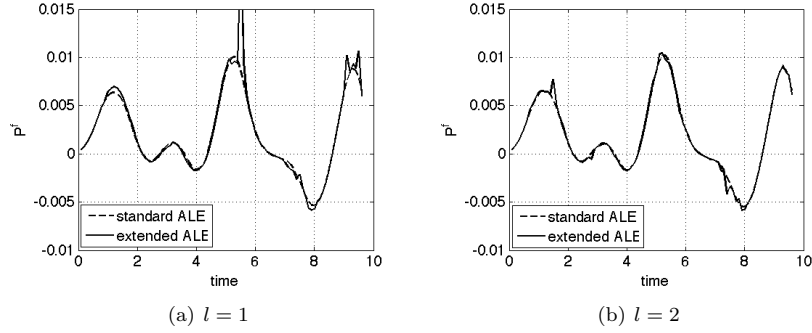


Figure 9: Comparison of discrete power exchanged at the interface from the fluid side  $P^f$ , defined by (31), computed with a standard ALE vs. our extended ALE method on mesh  $l = 1$ , shown in panel (a), and on mesh  $l = 2$ , shown in panel (b).

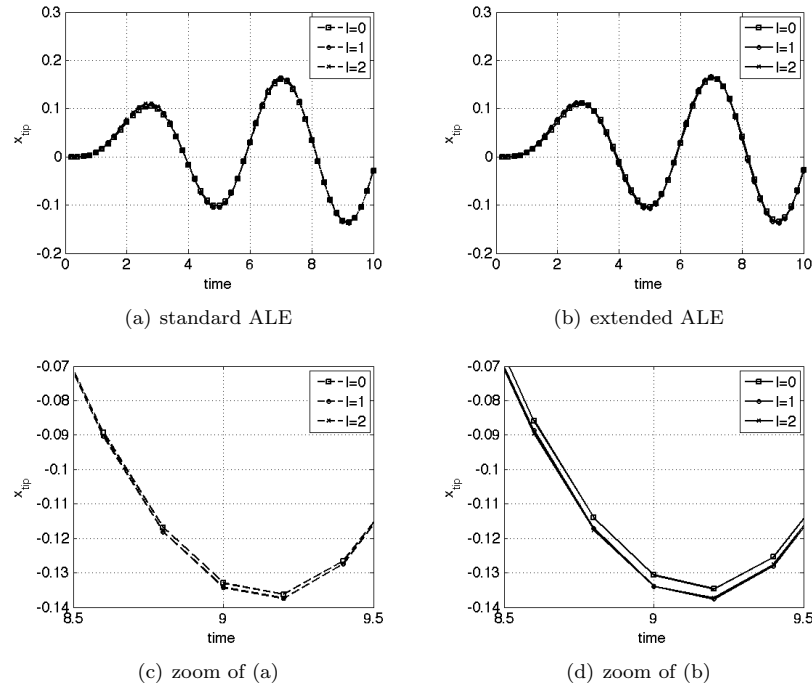


Figure 10: Horizontal component of the beam tip movement computed with a standard ALE method, shown in panel (a), and our extended ALE method, shown in panel (b), for different meshes. A zoomed view of (a) and (b) is reported in (c) and (d), respectively.

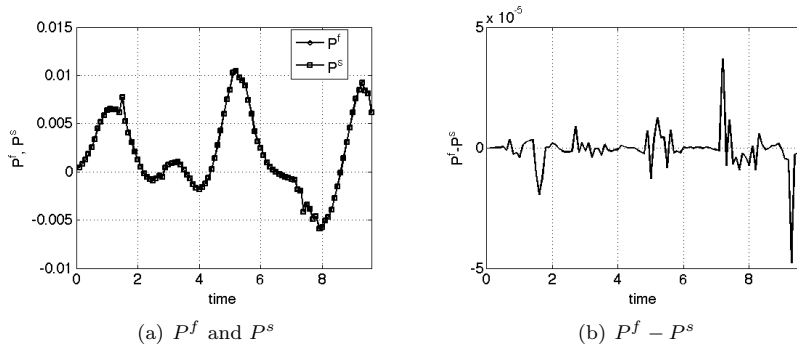


Figure 11: Extended ALE method, mesh  $l = 2$ : (a) discrete power exchanged at the interface from the fluid side  $P^f$ , defined in (31), and from the structure side  $P^s$ , defined in (32), over time; (b) the difference  $P^f - P^s$ .

time interval  $[0, 10]$  s, is plotted in Fig. 10(a). The corresponding graph obtained with the extended ALE method is shown in Fig. 10(b). Since one can hardly see any difference in the results computed with the three meshes, we report in Fig. 10(c) and 10(d) a zoomed view of Fig. 10(a) and 10(b), respectively. For both ALE methods, mesh independence is reached at the second mesh refinement. In fact, we see in Fig. 10(c) and 10(d) that the beam tip movement computed by both ALE methods on meshes  $l = 1$  and  $l = 2$  are superimposed.

**Power exchange quantification.** Next, we quantify the unbalance in the power exchange at the interface. As explained at the end of Sec. 4.3, at each time  $t^{n+1}$  the powers exchanged at the interface from the fluid side  $P^{f,n+1}$  and from the structure side  $P^{s,n+1}$  are not necessarily equal. In Fig. 11(a), we plot the powers  $P^f$  and  $P^s$  computed by the extended ALE method with mesh  $l = 2$  over the time interval under consideration, while in Fig. 11(b) we show the difference  $P^f - P^s$ . In Fig. 11(b), we see that over a long time interval the difference between the two powers exchanged at the interface is of the order of  $10^{-5}$  g cm/s<sup>3</sup>. This corresponds to 0.1% of the power value, which is of the order of  $10^{-2}$  g cm/s<sup>3</sup>, as shown in Fig. 11(a). Such a small difference in  $P^f$  and  $P^s$  does not endanger stability.

### 5.3. Test 3: Dirichlet-Neumann sub-iterations

This test is aimed at assessing the effectiveness of Aitken's acceleration method when the structure is immersed in the fluid. For this purpose we consider the same boundary conditions as in Test 2, and we set the same value for the flexural stiffness  $EI = 0.05$  g/(cm s<sup>2</sup>), however, we let the structure density vary:  $\rho_s = 32, 16, 8, 4, 2, 1, 0.5$  g/cm. Recall that the fluid density is  $\rho_f = 1$  g/cm<sup>3</sup>. As noted earlier, we expect to see problems (instabilities) in the Dirichlet-Neumann approach in the cases when the structure is relatively light with respect to the fluid [12]. In the problems studied in this manuscript, this means that we can expect instabilities in the Dirichlet-Neumann sub-iterations when the ratio  $\rho_s/\rho_f$  approaches one (from above).

We use the mesh for the fluid subdomain with  $h_f = \sqrt{2}/4$  cm, and we track the number of Dirichlet-Neumann iterations over time without and with

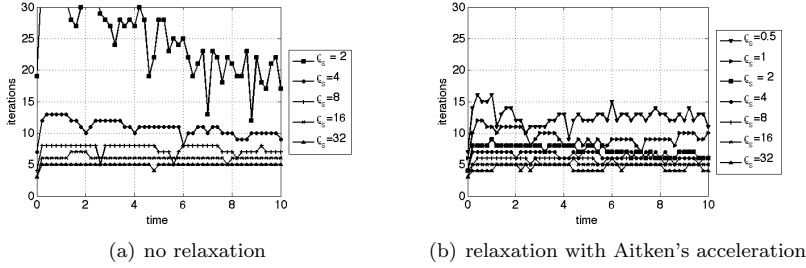


Figure 12: Extended ALE method: number of Dirichlet-Neumann iterations required to satisfy stopping criterion (14) over time (a) without and (b) with Aitken's acceleration parameters.

relaxation parameters given by Aitken's acceleration method. Fig. 12 report the results. The following conclusions can be obtained:

- When the structure is immersed in the fluid the number of Dirichlet-Neumann iterations increases as the structure density decreases, as expected. Such an increase in the number of iterations is more dramatic when no relaxation is used (see Fig. 12(a)).
- If no relaxation is used, the Dirichlet-Neumann algorithm ceases to converge when  $\rho_s$  reaches the value of  $\rho_f$  or goes below it.
- When the relaxation parameters are set by Aitken's acceleration method, the Dirichlet-Neumann algorithm converges regardless of the value of  $\rho_s$  and in much less iterations. For instance, for  $\rho_s = 2$  g/cm, the average number of Dirichlet-Neumann iterations over interval  $[0, 10]$  s is 25 when no relaxation is used and 7 when Aitken's acceleration method is adopted.

#### 5.4. Test 4: Large displacements

For the last test case, we impose at  $\Gamma_{in}$  a time dependent Poiseuille profile with maximum velocity which is four times larger than the one used in Test 2:

$$U(t) = \left(1 - \cos\left(\frac{\pi}{2}t\right)\right) \text{ cm/s,}$$

giving the Strouhal number 0.5, as in Test 2. The structural parameters are the same as in Test 2. The inlet boundary condition and the structural parameters are such that the induced motion of the beam displays large amplitude oscillations. See Fig. 14. The initial configuration of the beam is that of a straight, vertical line.

We use a mesh for the fluid subdomain with  $h_f = \sqrt{2}/16$  cm. We let the simulations with the standard and extended ALE method run until the standard ALE method breaks down due to excessive mesh distortion, which happens shortly after  $t = 6.5$  s.

Fig. 13 shows a comparison between standard and extended ALE method in terms of the  $x$  component of the beam tip movement and discrete power exchanged at the interface from the fluid side  $P^f$ , defined in (31). As long as the simulations with both ALE methods run, the computed  $x$  components of the movement of the beam tip are in excellent agreement (see Fig. 13(a)). The

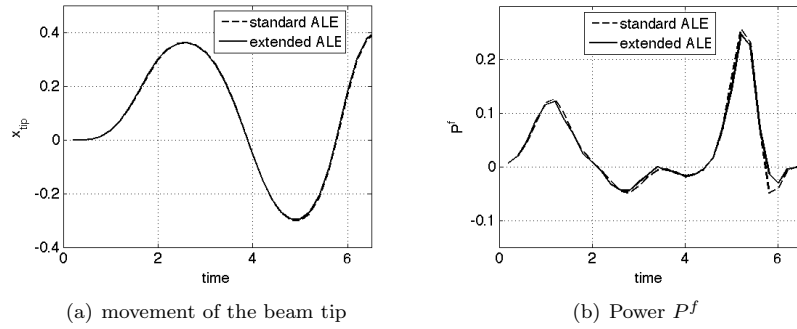


Figure 13: Comparison between standard and extended ALE method in terms of (a) the  $x$  component of the beam tip movement and (b) discrete power exchanged at the interface from the fluid side  $P^f$  (31).

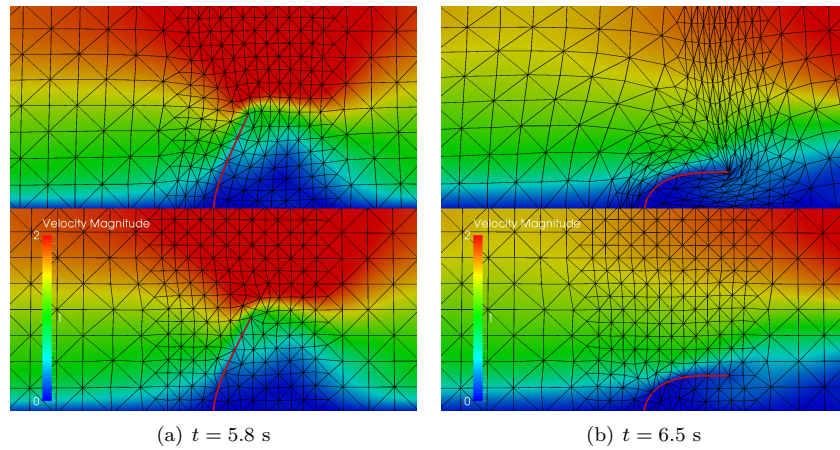


Figure 14: Test 4: fluid velocity magnitude and beam position computed with a standard ALE approach (top) and the extended ALE method (bottom) at the time (a)  $t = 5.8$  s and (b)  $t = 6.5$  s. The computational mesh is also shown.

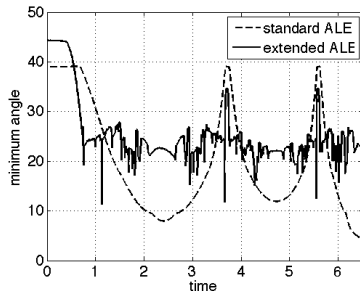


Figure 15: Minimum angle of the elements in the mesh given by the standard and extended ALE methods versus time.

discrete powers  $P^f$  computed by the two ALE methods are in good agreement until around  $t = 5.8$  s, which is close to when the simulation with the standard ALE method crashes.

In Fig. 14, we show a qualitative comparison of the beam position, together with the fluid velocity magnitude, computed with the standard and extended ALE methods at the time snapshots corresponding to  $t = 5.8$  s and  $t = 6.5$  s. Fig. 14 also displays the computational mesh at the selected times: notice the severe distortion of the mesh given by the standard ALE method occurring at time  $t = 6.5$  s. This will lead to the simulation break down within a few time steps. On the other side, the quality of the mesh given by the extended ALE method is still high (see Fig. 14(b), lower panel).

As a further proof of the different quality of the meshes given by the standard and extended ALE methods, we report in Fig. 15 the minimum angle of the elements over time. We see that the minimum angle in the meshes given by the standard ALE method occasionally drops below 10 degrees, while this never happens with the extended ALE method. In particular, the minimum angle in the mesh obtained with the standard ALE method is equal to 4 degrees at  $t = 6.5$  s. On the other hand, the average minimum angle for the meshes given by the extended ALE method oscillates around 23 degrees most of the time.

Unlike the simulation with the standard ALE method, the simulation with the extended ALE method does not crash over the time interval under consideration  $[0, 10]$  s.

## 6. Conclusions

Standard ALE methods for the simulation of fluid-structure interaction problems fail when the structural displacement is large. In this paper, we proposed an extended ALE method to overcome this limitation.

Our extended ALE method relies on a variational mesh optimization technique with an additional constraint to enforce the alignment of the structure interface with edges of the resulting triangulation. We combined this method with a Dirichlet-Neumann algorithm to simulate the interaction of an incompressible fluid with an inextensible beam. We adopted an acceleration technique based on Aitken's relaxation to allow convergence of the Dirichlet-Neumann algorithm when the structure density is comparable to, or smaller than, the fluid

density, and to speed up the convergence when the structure density is greater than the fluid density.

We performed several 2D tests to assess the proposed method. In particular, we showed that when the structural displacement is mild, the results given by our extended ALE method are in excellent agreement with the results given by a standard ALE method. On the other hand, when the structural displacement is large, and a standard ALE method fails, we showed that the quality of the mesh given by the extended ALE method remains high, thereby allowing full computer simulations of the underlying problem.

Due to the simplicity and their instructive nature, the test problems considered in this manuscript could be used as benchmark problems in the development of numerical tools for the computer simulation of FSI problems involving immersed structures with large displacement, such as, e.g., heart valve problems.

### Acknowledgements

The research presented in this work was carried out during Basting's visit at University of Houston, supported by National Science Foundation (NSF) grant DMS-1318763 (Canic) and Cullen Chair funds. This research has been supported in part by the NSF under grants DMS-1311709 (Canic), DMS-1262385 and DMS-1109189 (Canic and Quaini), and by the Texas Higher Education Board (ARP-Mathematics) 003652-0023-2009 (Canic and Glowinski).

### References

- [1] M. Astorino, J.-F. Gerbeau, O. Pantz, and K.-F. Traoré. Fluid-structure interaction and multi-body contact: Application to aortic valves. *Computer Methods in Applied Mechanics and Engineering*, 198(45-46):3603 – 3612, 2009.
- [2] F.P.T. Baaijens. A fictitious domain/mortar element method for fluid-structure interaction. *Int. J. Numer. Meth. Fl.*, 35(7):743–761, 2001.
- [3] E. Bänsch, J. Paul, and A. Schmidt. An ALE finite element method for a coupled Stefan problem and Navier-Stokes equations with free capillary surface. *International Journal for Numerical Methods in Fluids*, 2012.
- [4] S. Basting and R. Prignitz. An interface-fitted subspace projection method for finite element simulations of particulate flows. *Computer Methods in Applied Mechanics and Engineering*, 267(0):133 – 149, 2013.
- [5] S. Basting, A. Quaini, R. Glowinski, and S. Canic. Comparison of time discretization schemes to simulate the motion of an inextensible beam. *Numerical Analysis & Scientific Computing Preprint Series 25*, University of Houston, 2013. [http://www.mathematics.uh.edu/docs/math/NASC-preprint-series/2013.2014/Preprint\\_No13-25.pdf](http://www.mathematics.uh.edu/docs/math/NASC-preprint-series/2013.2014/Preprint_No13-25.pdf).
- [6] S. Basting and M. Weismann. A hybrid level set/front tracking approach for finite element simulations of two-phase flows. *Journal of Computational and Applied Mathematics*, In Press, 2013.

- [7] S. Basting and M. Weismann. A hybrid level set/front tracking finite element approach for fluid-structure interaction and two-phase flow applications. *Journal of Computational Physics*, 255:228 – 244, 2013.
- [8] K. Bäumlner and E. Bänsch. A subspace projection method for the implementation of interface conditions in a single-drop flow problem. *Journal of Computational Physics*, 252:438 – 457, 2013.
- [9] B. Bejanov, J.L. Guermond, and P.D. Minev. A grid-alignment finite element technique for incompressible multicomponent flows. *Journal of Computational Physics*, 227(13):6473 – 6489, 2008.
- [10] J.-F. Bourgat, M. Dumay, and R. Glowinski. Large displacement calculations of inextensible pipelines by finite element and nonlinear programming methods. *SIAM J. Sci. Stat. Comput.*, 1:34–81, 1980.
- [11] M. Bukac, S. Canic, R. Glowinski, J. Tambaca, and A. Quaini. Fluid-structure interaction in blood flow capturing non-zero longitudinal structure displacement. *Journal of Computational Physics*, 235:515–541, 2013.
- [12] P. Causin, J.F. Gerbeau, and F. Nobile. Added-mass effect in the design of partitioned algorithms for fluid-structure problems. *Comput. Methods Appl. Mech. Engrg*, 194(42-44):4506–4527, 2005.
- [13] G.H. Cottet, E. Maitre, and T. Milcent. Eulerian formulation and level set models for incompressible fluid-structure interaction. *Esaim. Math. Model. Numer. Anal.*, 42:471–492, 2008.
- [14] T.A. Davis. Algorithm 832: Umfpack V4.3—an unsymmetric-pattern multifrontal method. *ACM Trans. Math. Softw.*, 30(2):196–199, 2004.
- [15] T.A. Davis and I.S. Duff. A combined unifrontal/multifrontal method for unsymmetric sparse matrices. *ACM Trans. Math. Softw.*, 25(1):1–20, 1999.
- [16] J. Donea, S. Giuliani, and J.P. Halleux. An Arbitrary Lagrangian-Eulerian finite element method for transient dynamic fluid-structure interactions. *Computer Methods in Applied Mechanics and Engineering*, 33(1-3):689 – 723, 1982.
- [17] N. Diniz dos Santos, J.-F. Gerbeau, and J.-F. Bourgat. A partitioned fluid-structure algorithm for elastic thin valves with contact. *Comput. Methods Appl. Mech. Engrg*, 197:1750–1761, 2008.
- [18] J. Dukowicz and J. Kodis. Accurate Conservative Remapping (Rezoning) for Arbitrary Lagrangian-Eulerian Computations. *SIAM Journal on Scientific and Statistical Computing*, 8(3):305–321, 1987.
- [19] H. Fang, Z. Wang, Z. Lin, and M. Liu. Lattice Boltzmann method for simulating the viscous flow in large distensible blood vessels. *Phys. Rev. E.*, 65(5):051925–1–051925–12, 2002.
- [20] C. Farhat, M. Lesoinne, and P. Le Tallec. Load and motion transfer algorithms for fluid/structure interaction problems with non-matching discrete interfaces: Momentum and energy conservation, optimal discretization and application to aeroelasticity. *Computer Methods in Applied Mechanics and Engineering*, 157(12):95 – 114, 1998.

- [21] Z.G. Feng and E.E. Michaelides. The immersed boundary-lattice Boltzmann method for solving fluid-particles interaction problems. *J. Comp. Phys.*, 195(2):602–628, 2004.
- [22] L. Formaggia, A. Quarteroni, and A. Veneziani. *Cardiovascular Mathematics*, volume 1 of *Modeling, Simulation and Applications*. Springer, 2009.
- [23] M. Fortin and R. Glowinski. *Augmented Lagrangian Methods: Application to the Numerical Solution of Boundary Value Problem*. North-Holland, Amsterdam, 1983.
- [24] R. Glowinski and M. Holmstrom. Constrained motion problems with applications by nonlinear programming methods. *Surv. Math. Ind.*, 5:75–108, 1995.
- [25] R. Glowinski, T.-W. Pan, T.I. Hesla, and D.D. Joseph. A distributed Lagrange multiplier/fictitious domain method for particulate flows. *International Journal of Multiphase Flow*, 25(5):755 – 794, 1999.
- [26] R. Glowinski, T.W. Pan, and J. P eriaux. A fictitious domain method for external incompressible viscous flow modelled by Navier-Stokes equations. *Methods Appl. Mech. Engrg.*, 111:133–148, 1994.
- [27] R. Glowinski and P. Le Tallec. *Augmented Lagrangian and Operator-Splitting Methods in Nonlinear Mechanics*. SIAM, Philadelphia, 1988.
- [28] J. De Hart, F.P.T. Baaijens, G.W.M. Peters, and P.J.G. Schreurs. A computational fluid-structure interaction analysis of a fiber-reinforced stentless aortic valve. *Journal of Biomechanics*, 36(5):699 – 712, 2003.
- [29] J. De Hart, G.W.M. Peters, P.J.G. Schreurs, and F.P.T. Baaijens. A three-dimensional computational analysis of fluid-structure interaction in the aortic valve. *Journal of Biomechanics*, 36(1):103 – 112, 2003.
- [30] H. Hu, N.A. Patankar, and M.Y. Zhu. Direct numerical simulations of fluid-solid systems using the Arbitrary Lagrangian-Eulerian technique. *Journal of Computational Physics*, 169(2):427 – 462, 2001.
- [31] T. J. R. Hughes, W. Liu, and T. K. Zimmermann. Lagrangian-Eulerian finite element formulation for incompressible viscous flows. *Computer Methods in Applied Mechanics and Engineering*, 29(3):329 – 349, 1981.
- [32] M. Krafczyk, M. Cerrolaza, M. Schulz, and E. Rank. Analysis of 3D transient blood flow passing through an artificial aortic valve by Lattice-Boltzmann methods. *J. Biomech.*, 31(5):453–462, 1998.
- [33] U. K uttler and W.A. Wall. Fixed-point fluid-structure interaction solvers with dynamic relaxation. *Computational Mechanics*, 43(1):61–72, 2008.
- [34] R. Loubere, P.-H.i Maire, M. Shashkov, J. Breil, and S. Galera. Reale: A reconnection-based arbitrary-lagrangian–eulerian method. *Journal of Computational Physics*, 229(12):4724 – 4761, 2010.

- [35] L.G. Margolin and M. Shashkov. Second-order sign-preserving conservative interpolation (remapping) on general grids. *Journal of Computational Physics*, 184(1):266 – 298, 2003.
- [36] D.P. Mok and W.A. Wall. Partitioned analysis schemes for transient interaction of incompressible flows and nonlinear flexible structures. In *Trends in computational structural mechanics (W.A. Wall, K.U. Bletzinger and K. Schweizerhof, Eds.)*, CIMNE, Barcelona, Spain, 2001.
- [37] F. Nobile. *Numerical Approximation of Fluid-Structure Interaction Problems with Application to Haemodynamics*. PhD thesis, École Polytechnique Fédérale de Lausanne, 2001.
- [38] C. S. Peskin. Numerical analysis of blood flow in the heart. *Journal of Computational Physics*, 25(3):220 – 252, 1977.
- [39] C. S. Peskin. The Immersed Boundary method. *Acta Numer.*, 11:479–517, 2002.
- [40] C.S. Peskin and D.M. McQueen. A three-dimensional computational method for blood flow in the heart i. Immersed elastic fibers in a viscous incompressible fluid. *Journal of Computational Physics*, 81(2):372 – 405, 1989.
- [41] R. Prignitz and E. Bänsch. Particulate flows with the subspace projection method. *Journal of Computational Physics*, 260(0):249 – 272, 2014.
- [42] A. Quarteroni and A. Valli. *Domain Decomposition Methods for Partial Differential Equations*. Oxford Science Publications, 1999.
- [43] M. Rumpf. A variational approach to optimal meshes. *Numerische Mathematik*, 72:523–540, 1996.
- [44] P. Le Tallec and J. Mouro. Fluid-structure interaction with large structural displacements. *Comput. Methods Appl. Mech. Engrg.*, 190:3039–3067, 2001.
- [45] R. van Loon, P. D. Anderson, J. de Hart, and F. P. T. Baaijens. A combined fictitious domain/adaptive meshing method for fluid-structure interaction in heart valves. *International Journal for Numerical Methods in Fluids*, 46(5):533–544, 2004.
- [46] R. van Loon, P.D. Anderson, F.P.T. Baaijens, and F.N. van de Vosse. A three-dimensional fluid-structure interaction method for heart valve modelling. *Comptes Rendus Mécanique*, 333(12):856 – 866, 2005.
- [47] X. Wang and W. Liu. Extended immersed boundary method using FEM and RKPM. *Methods Appl. Mech. Engrg.*, 193:1305 – 1321, 2004.
- [48] M. Weismann. The hybrid level-set front-tracking approach. Master’s thesis, Friedrich-Alexander University Erlangen-Nuremberg, 2012.
- [49] L. Zhang, A. Gerstenberger, X. Wang, and W.K. Liu. Immersed finite element method. *Methods Appl. Mech. Engrg.*, 193:2051 – 2067, 2004.